Fourier analyses of commensurability oscillations in Fibonacci lateral superlattices

Akira Endo* and Yasuhiro Iye
Institute for Solid State Physics, University of Tokyo, 5-1-5 Kashiwanoha, Kashiwa, Chiba 277-8581, Japan
(Received 3 May 2008; published 20 August 2008)

Magnetotransport measurements have been performed on Fibonacci lateral superlattices—two-dimensional electron gases subjected to a weak potential modulation arranged in the Fibonacci sequence *LSLLSLS*… with $L/S=\tau$ (golden ratio). Complicated commensurability oscillation (CO) is observed, which can be accounted for as a superposition of a series of COs each arising from a sinusoidal modulation representing the characteristic length scale of one of the self-similar generations in the Fibonacci sequence. Individual CO components can be separated out from the magnetoresistance trace by performing a numerical Fourier band-pass filter. From the analysis of the amplitude of a single-component CO thus extracted, the magnitude of the corresponding Fourier component in the potential modulation can be evaluated. By examining all the Fourier contents observed in the magnetoresistance trace, the profile of the modulated potential seen by the electrons can be reconstructed with some remaining ambiguity about the interrelation of the phase between different components.

DOI: 10.1103/PhysRevB.78.085311 PACS number(s): 73.23.Ad, 75.47.Jn, 61.44.Br

I. INTRODUCTION

A GaAs/AlGaAs-based high mobility two-dimensional electron gas (2DEG) combined with modern electron-beam (EB) lithography allows us to fabricate a device in which electrons travel through an artificially designed environment over a sufficiently long distance before being scattered by impurities.[1] A prototypical example of such devices is a lateral superlattice (LSL), where a periodic modulation of electrostatic potential is introduced to a 2DEG. The periodic modulation can be either one dimensional (1D) or two dimensional (2D), exemplifying the versatility of LSLs compared to more conventional vertical superlattices. The planar geometry of a LSL is well suited for experimental studies of the transport properties and therefore the magnetotransport of both 1D and 2D LSLs, with the magnetic field B applied perpendicular to the 2DEG plane, has been the subject of extensive studies [see, e.g., Refs. 2–15 and Refs. 16–20 (and references therein) for 1D and 2D LSLs, respectively].

In a 1D LSL, a number of phenomena are known in the magnetotransport, including low-field positive magnetoresistance (PMR),[2] commensurability oscillation (CO) originating from the commensurability between the cyclotron radius and the modulation period,[3] quantum interference of closed orbits,[14] and geometric resonance of open orbits.[15] The periodic modulation in a 1D LSL can be replaced by a quasiperiodic one without appreciable technical difficulties. Quasiperiodic structures are characterized by long-range order without translational symmetry and constitute intriguing intermediate states situated between perfect periodicity and disorder.[21] A wealth of exotic properties, such as localized or critical wave functions and a Cantor-set spectrum, are theoretically predicted[22–24] with varieties of experimental systems devoted for their exploration.[25–39] It is therefore of great interest to perceive how the magnetotransport phenomena observed in a periodic 1D LSL are altered (or remain unaltered) in a quasiperiodic 1D LSL, as well as to search for phenomena peculiar to the quasiperiodic systems. The Fibonacci sequence typifies quasiperiodic systems in 1D. The present authors have been studying the magnetotransport of LSL samples with the potential modulation arranged in the Fibonacci sequence—the Fibonacci LSL (FLSL). In previous publications, we briefly reported complicated CO and geometric resonance of open orbits observed in FLSLs,[40] as well as the enhancement of zero-field resistivity, followed by strong negative magnetoresistance for FLSLs with short-length-scale modulation approaching the Fermi wavelength.[41] In the present paper, we focus on the quantitative Fourier analysis of CO. We will show that the magnitudes of individual Fourier components that constitute the potential modulation can be determined by the analysis. Detailed knowledge of the potential profile thus obtained forms the basis for understanding the electronic properties or phenomena in FLSLs to be explored in the future studies.

The paper is organized as follows. In Sec. II, the CO for a simple sinusoidal periodic LSL and its extension to systems with multiple Fourier components are briefly reviewed in order to prepare for later application to the analysis of FLSLs. Details of the samples and the experimental setup are described in Sec. III. The main subject of the paper is presented in Sec. IV where we delineate the prescription to single out CO corresponding to a particular Fourier component from the magnetoresistance trace of a FLSL and to deduce the amplitude of the potential modulation for the component. We further make an attempt to reconstruct the potential profile by exploiting the phases of the Fourier components inferred by examining the origin of each component. Discussion on the limitation in the accuracy of the potential profile thus determined is given in Sec. V followed by the concluding remarks in Sec. VI.

II. COMMENSURABILITY OSCILLATION IN PERIODIC LATERAL SUPERLATTICES

In a periodic 1D LSL, the oscillatory component of the resistivity in the CO $\delta\rho_{xx}^{g}(B)$ is well understood quantitatively. We take the x direction to be the direction of the modulation $V(x)$ and of the current for the resistivity measurement and the xy plane to be the plane of the 2DEG with B applied along the z axis throughout this paper. For a sinu-

soidal modulation $V(x)=V_g\cos(gx)$ with period $a=2\pi/g$ and with amplitude V_g much smaller than the Fermi energy E_F, $\delta\rho_{xx}^g(B)$ has been experimentally shown to be accurately described by a simple analytical formula,[42,43]

$$\frac{\delta\rho_{xx}^g(B)}{\rho_0 A(T/T_g)} = \gamma A\left(\frac{\pi}{\mu_w B}\right) g V_g^2 B \sin(2gR_c), \tag{1}$$

with

$$\gamma = \frac{1}{2(2\pi)^{3/2}}\left(\frac{h}{e}\right)^{-1}\left(\frac{e\hbar}{2m^*}\right)^{-2}\frac{\mu^2}{n_e^{3/2}}, \tag{2}$$

$\rho_0=\rho_{xx}(0)$, $A(X)=X/\sinh(X)$, $k_BT_g=(1/2\pi)(k_F/g)\hbar\omega_c$, m^* the electron effective mass ($0.067m_e$ for GaAs), $\omega_c=eB/m^*$ the cyclotron angular frequency, $R_c=\hbar k_F/eB$ the cyclotron radius, $k_F=\sqrt{2\pi n_e}$ the Fermi wave number, and μ and n_e represent the mobility and the density of the electrons, respectively. The factor $A(\pi/\mu_wB)$ in Eq. (1) is the damping factor arising from the scattering of electrons out of their cyclotron orbit with μ_w an appropriate mobility usually identifiable with the quantum mobility μ_q that describes the damping of the Shubnikov-de Haas (SdH) oscillation. Apart from the thermal and scattering damping factors $A(T/T_a)$ and $A(\pi/\mu_wB)$, Eq. (1) can be deduced from a physically transparent semiclassical picture.[44] Electrons acquire a drift velocity $v_{d,y}(x)=-E(x)/B$ in the simultaneous presence of an electric field $E(x)=(1/e)dV(x)/dx$ and a magnetic field B. The average of the drift velocity over one cycle of the cyclotron orbit,

$$\overline{v_{d,y}}(x_0) = \frac{1}{2\pi}\int_0^{2\pi} d\theta v_{d,y}(x_0+R_c\cos\theta)$$

$$= \frac{gV_g}{eB}\sin(gx_0)J_0(gR_c), \tag{3}$$

oscillates with B reflecting the commensurability between a and R_c with the amplitude depending on the guiding center position x_0. Here, $J_0(X)$ represents the Bessel function of order zero. The conductivity deriving from the commensurability effect $\delta\sigma_{yy}$ is obtained by further averaging the square $\overline{v_{d,y}}^2(x_0)$ over x_0 (averaging over one modulation period suffices for a periodic LSL) and substituting the resultant $\langle\overline{v_{d,y}}^2\rangle$ in the Einstein's relation $\delta\sigma_{yy}=e^2(m^*/\pi\hbar^2)(\tau_m\langle\overline{v_{d,y}}^2\rangle)$ with $\tau_m=(e/m^*)\mu$ the (momentum relaxation) scattering time. The corresponding resistivity is obtained by inverting the conductivity tensor $\delta\rho_{xx}/\rho_0=(\omega_c\tau_m)^2\delta\sigma_{yy}/\sigma_0$ with $\sigma_0=n_ee^2\tau_m/m^*$ for $(\omega_c\tau_m)^2=(\mu B)^2\gg 1$. This, with the Bessel function replaced by its asymptotic expression $J_0(X)\simeq\sqrt{2/\pi X}\cos(X-\pi/4)$, coincides with Eq. (1) except for nonoscillatory term linear in B and the damping factors. The scattering damping factor can be incorporated within the semiclassical picture by the Boltzmann equation approach.[45] The thermal damping factor results from standard treatment of the blurred edge of the Fermi-Dirac distribution function. Virtually the same result [with $A(T/T_a)$ but without $A(\pi/\mu_wB)$] is arrived at by quantum-mechanical calculations that treat $V(x)$ by the first-order perturbation theory.[46,47]

By fitting Eq. (1) to an experimentally obtained CO trace, unknown parameters of the LSL sample under investigation can be deduced. It can readily be seen from Eq. (1) that the oscillation is periodic in $1/B$ with minima taking place at the conditions,

$$\frac{gR_c}{\pi} = \frac{B_g}{B} = n - \frac{1}{4} \quad (n=1,2,3,\ldots). \tag{4}$$

From the frequency B_g, the wave number $g=\pi eB_g/\hbar k_F$ of the potential modulation (if unknown) is revealed using the n_e determined either by the Hall resistivity or by the SdH oscillation. The parameters V_g and μ_w are obtained from the oscillation amplitude. Fitting the experimental values of $|\delta\rho_{xx}^g(B)/\rho_0A(T/T_g)|$ at the extrema to the function $C/\sinh(B_w/B)$ employing C and B_w as fitting parameters, we get $V_g=\sqrt{C/(B_w\gamma g)}$ and $\mu_w=\pi/B_w$, where γ is evaluated by Eq. (2) using experimentally obtained parameters μ and n_e.

Extension of the above argument to general potentials of the form $V(x)=\Sigma_gV_g\cos(gx+\phi_g)$ is straightforward. The resulting conductivity was shown, using the quantum-mechanical Kubo formula, to be simply additive;[48] it can also readily be shown by the semiclassical derivation presented above by noting that the cross terms in the square of the cycle-averaged drift velocity $\overline{v_{d,y}}(x_0)=\Sigma_g(gV_g/eB)\sin(gx_0+\phi_g)J_0(gR_c)$ vanish upon averaging over x_0. The total oscillatory part of the CO thus reads

$$\delta\rho_{xx}^{\text{tot}} = \sum_g \delta\rho_{xx}^g, \tag{5}$$

with $\delta\rho_{xx}^g$ given by Eq. (1). The phase ϕ_g is equivalent to the shift of the guiding center by ϕ_g/g and therefore does not appear in Eq. (5) obtained by the averaging over x_0; the information on the phase is lost in the resistivity. For a (nonsinusoidal) periodic potential that includes higher harmonics,[49] the g in the summation contains only integer multiples of the fundamental component g_0, i.e., $g=\lambda g_0$ ($\lambda=1,2,3,\ldots$). However, Eq. (5) is applicable to a more general potential that involves g's with the ratio λ given by irrational numbers as is the case in our present FLSL samples. Once experimentally measured $\delta\rho_{xx}^{\text{tot}}$ is decomposed into its constituent $\delta\rho_{xx}^g$'s, the corresponding V_g's can be obtained following the prescription for a sinusoidal modulation described above. This is the main subject of the present paper that will be demonstrated in what follows.

III. EXPERIMENTAL DETAILS

The Fibonacci sequence *LSLLSLSLLSL*… is generated by first preparing two unit lengths L and S with the ratio $L/S=\tau=(1+\sqrt{5})/2=1.61803\ldots$ (the golden ratio) and then repeating the inflation rules $S\rightarrow L$ and $L\rightarrow LS$ starting from a single S. In a FLSL, modulation arranged in the Fibonacci sequence is introduced to a 2DEG. The samples are fabricated from conventional GaAs/AlGaAs single heterostructure 2DEG wafers ($\mu=50-100$ m^2/Vs and $n_e=1.7-3.0\times10^{15}$ m^{-2} varied by light-emitting diode illumination) with the heterointerface residing at the depth of 90 nm from the surface. The electrostatic potential modulation is introduced by exploiting the strain-induced piezoelectric effect;[50] the strain being generated upon cooling by the slabs of negative

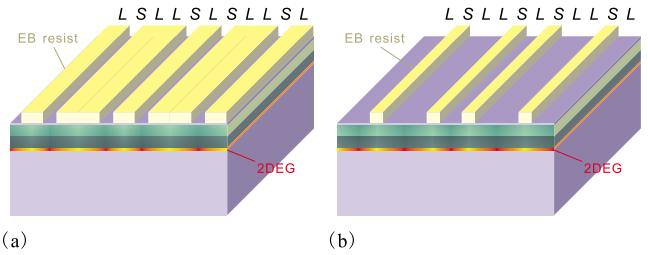

FIG. 1. (Color online) Schematic illustrations of the FLSL samples. (a) and (b) represent *L*-type and *S*-type samples, respectively.

EB resist[42] placed on the surface selectively on either of the *L* (*L*-type FLSL) or *S* sites (*S*-type FLSL) as depicted in Fig. 1. Seven *L*-type and three *S*-type samples with varying unit lengths tabulated in Table I are examined. The accuracy of the actual width of the resist slabs is estimated from the scanning electron micrographs to be roughly within 10% of the ideal values.

A Hall-bar pattern with two sets of voltage probes are employed for the samples (as illustrated in the inset of Fig. 2) allowing for the simultaneous measurement of the unpatterned plain 2DEG adjacent to the FLSL for reference. The width of the Hall bars and the center-to-center distance between the voltage probes are 14 and 40 μm, respectively. Thus, the FLSLs contain from 140 (sample 110*S*) to 290 (sample 40*L*) segments of the *S* site. The main panel of Fig. 2 shows a typical magnetoresistance trace of a FLSL along with that of the adjacent plain 2DEG. The measurement is carried out by standard low-frequency ac lock-in technique. We have checked that the microfabrication process to introduce the modulation does not degrade the mobility and also does not alter the electron density (as is evident by comparing the SdH oscillations observed in the two traces for $B \gtrsim 0.5$ T). In the FLSL, the CO is observed for $B \gtrsim 0.05$ T following the low-field PMR. The complicated nonmonotonic nature of the CO in the FLSL is immediately evident by the comparison with the CO of a periodic LSL also plotted in Fig. 2 for reference. Quantitative analysis of the CO in FLSLs will be presented in Sec. IV A.

TABLE I. List of samples. $\langle \Delta x_{\mathrm{res}} \rangle$ denotes the average distance between the centers of adjacent resist slabs.

Sample ID	*L* (nm)	*S* (nm)	$\langle \Delta x_{\mathrm{res}} \rangle$ (nm)	Type
90*L*	104	64	231	*L*
70*L*	81	50	180	*L*
60*L*	69	43	154	*L*
55*L*	63	39	141	*L*
50*L*	58	36	129	*L*
45*L*	52	32	116	*L*
40*L*	46	28	103	*L*
110*S*	127	78	283	*S*
100*S*	115	71	257	*S*
90*S*	104	64	231	*S*

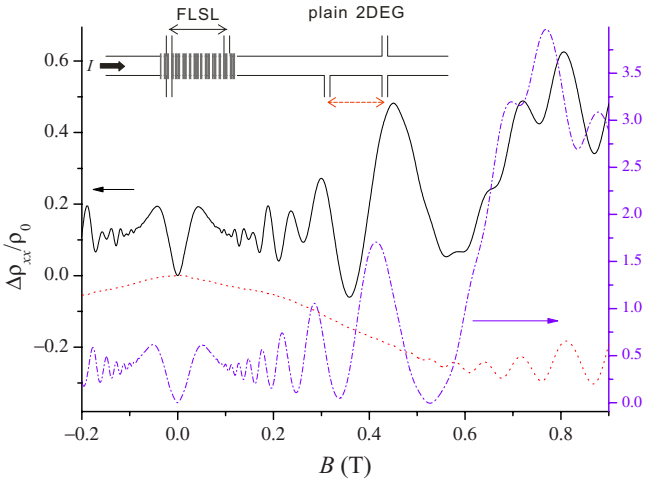

FIG. 2. (Color online) Magnetoresistance traces of a FLSL (solid line) and the adjacent plain 2DEG (dotted line) taken at 4.2 K from sample 70*L* (left axis). Magnetoresistance trace for a periodic LSL (a=184 nm, V_g=0.3 meV) is also shown for comparison (dash-dotted line with negative offset—right axis). The inset schematically depicts the configuration of the sample.

IV. FOURIER ANALYSES OF THE COMMENSURABILITY OSCILLATION

A. Separation of Fourier components and the analyses of the CO amplitudes

In this section, we describe (taking sample 70*L* as an example) the procedure to separate Fourier components from a magnetoresistance trace $\Delta\rho_{xx}(B)/\rho_0 = (\rho_{xx}(B) - \rho_0)/\rho_0$ as shown in Fig. 2 and to analyze the CO amplitude of each Fourier content thus singled out. The first step is to subtract the slowly varying background to obtain the oscillatory part. In the case of a periodic LSL, the background can readily be defined as the average of the upper and lower envelope curves;[42] since the CO amplitude decreases monotonically with decreasing magnetic field, the envelope curves obtained as spline curves that connect maxima or minima and hence their average are also monotonic. A similar approach is not applicable for FLSLs having nonmonotonic envelope curves. We instead make use of the numerical differentiation by B that effectively operates as a high pass filter. The second derivative successfully eliminates the slowly varying part as can be seen in Fig. 3(a), which shows $(d^2/dB^2)[\Delta\rho_{xx}(B)/\rho_0]$ plotted against $1/B$.

The Fourier transform of Fig. 3(a) presented in Fig. 4 displays discrete peaks. This indicates that the beating of the oscillation in Fig. 3(a) can be viewed as resulting from the superposition of a number of components periodic in $1/B$. A peak originating from the SdH effect is also observed. The positions of the principal peaks marked in Fig. 4 by f_j (j =5,4,3,2 and a small trace for j=1) are mutually related by $f_j/f_{j+1}=\tau$, namely, the positions of adjacent peaks are scaled by the golden ratio τ. The other two minor peaks bear the relations $f_{2,-2}=2f_4$ and $f_{0,2}=2f_3$. These peaks can be explained in terms of the reciprocal lattice for a 1D Fibonacci sequence.

It is well known that quasiperiodic structures show a set of discrete sharp diffraction spots despite the absence of defi-

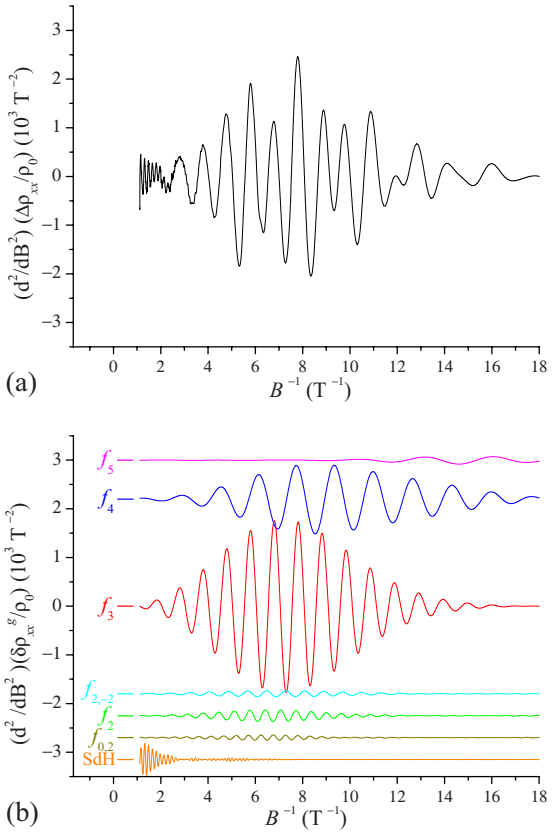

FIG. 3. (Color online) (a) The plot of $(d^2/dB^2)(\Delta\rho_{xx}/\rho_0)$ vs $1/B$. (b) Harmonic components of (a) obtained by performing Fourier band-pass filters. Corresponding windows are shown in Fig. 4. The left axis is for f_3 and other traces are offset for clarity.

nite periodicity.[51] The reciprocal lattice of a 1D Fibonacci lattice can readily be found by noting that the Fibonacci sequence can be generated also by the projection of a 2D square lattice, with the lattice constant $\sqrt{1+\tau^2}S$, onto a line having the slope equal to $1/\tau$; the reciprocal lattice or equivalently the position of peaks in the Fourier transform is given by $g_{m,n}=(2\pi/S)f_{m,n}$ with

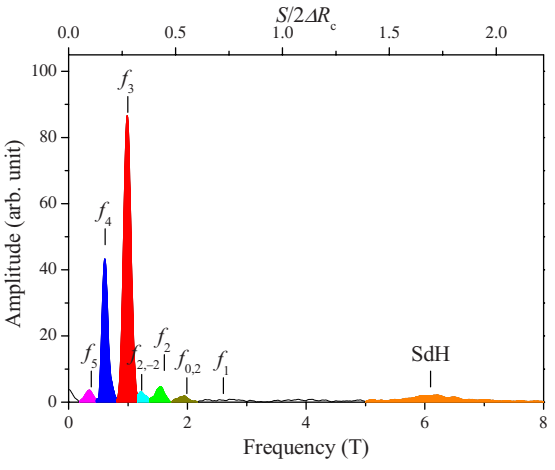

FIG. 4. (Color online) The Fourier spectrum of the trace of $(d^2/dB^2)(\Delta\rho_{xx}/\rho_0)$ vs $1/B$ shown in Fig. 3(a). The shaded areas indicate the windows employed in the band-pass filters in Fig. 3.

$$f_{m,n}=\frac{m\tau+n}{\tau+2}, \tag{6}$$

and m and n integers.[52] Although in principle $g_{m,n}$'s fill up the entire 1D reciprocal space, only a small fraction of them with smaller values of $|m|$ and $|n|$ have practically effective amplitudes of the structure factor—the detail of which depending on the actual profile of the potential.[53]

The above-mentioned principal sequence coincides with Eq. (6) with two successive Fibonacci numbers $m=F_{3-j}$ and $n=F_{2-j}$,

$$f_j=f_{F_{3-j},F_{2-j}}=\frac{\tau^{3-j}}{\tau+2}=\frac{\tau^{2-j}}{\sqrt{5}}, \tag{7}$$

if we translate the frequency B_g into $S/2\Delta R_c$, the inverse of the corresponding increment in the cyclotron diameter $2\Delta R_c=2\hbar k_F/eB_g$ taking S as the unit of the length (top axis in Fig. 4). Here the Fibonacci numbers F_n are defined by $F_0=0$, $F_1=1$, and $F_{n+2}=F_{n+1}+F_n$ for both positive and negative integers n and can be explicitly written as $F_n=[\tau^n-(-\tau)^{-n}]/\sqrt{5}$ (the Binet formula[54,55]). In Eq. (7), we made use of an identity $\tau^n=\tau F_n+F_{n-1}$. The two minor peaks are also expressed in terms of Eq. (6).

The peak at $f_{m,n}$ corresponds to the modulation wave number $g=(2\pi/S)f_{m,n}$ or the modulation period $S/f_{m,n}$. Therefore Fig. 4 reveals that the profile of the modulation is mainly composed of the superposition of multiple incommensurate components having the periods S/f_j; the periods successively scaled by an irrational number τ. Physical interpretation of these periods will be presented in Sec. IV B.

The trace in Fig. 3(a) can be decomposed into its Fourier components by performing a numerical Fourier band-pass filter. The resultant components obtained by applying the windows that encompass the corresponding peaks (shaded areas in Fig. 4) are displayed in Fig. 3(b). The next step is to restore the resistivity $\delta\rho^g_{xx}$ from its second derivative. This can be readily done by numerically integrating the second derivative [replot of Fig. 3(b) against B] by B twice. The decomposed Fourier components of the CO (and also the SdH oscillation) thus obtained are plotted in Fig. 5. The summation of all the observed components (thick dashed curve) restores the oscillatory part of the original magnetoresistance trace (thick solid curve) with high fidelity, indicating that we are on the right track. As shown in Fig. 6(a), the plot of the index of the extrema in each CO component versus their position in $1/B$ falls on a line with the slope B_g that coincides with the peak position of the FFT spectrum (lower axis in Fig. 4) within experimental error and with the ordinate intercept $\sim 1/4$—as expected from Eq. (4)—thereby confirming that adequate CO components are extracted. Here we assigned half-integer indices to the maxima.

The final step is to deduce the modulation amplitude V_g from the amplitude of CO following the procedure described in Sec. II. The values of $|\delta\rho^g_{xx}(B)/\rho_0 A(T/T_g)|$ at the extrema are plotted in Fig. 6(b) for the three major components f_2, f_3, and f_4. As can be seen, the function $C/\sinh(B_w/B)$ describes the behavior of the normalized amplitudes quite well. Fitting by the two parameters C and B_w can be carried out without

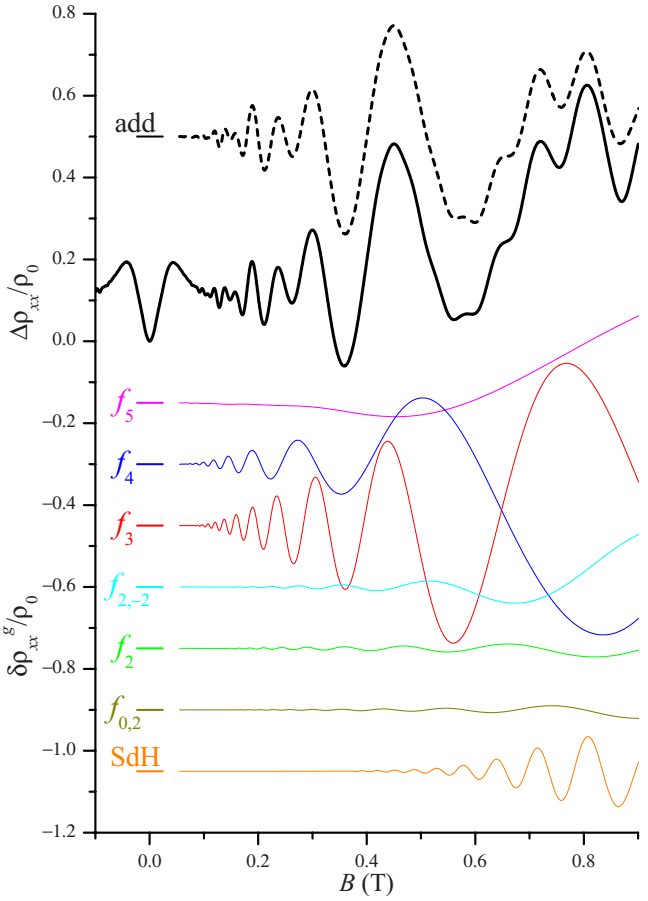

FIG. 5. (Color online) Experimental magnetoresistance trace (thick solid line), the Fourier components extracted by the procedure described in the text (thin solid lines with downward offsets), and the addition of the Fourier components (thick dashed line with upward offset).

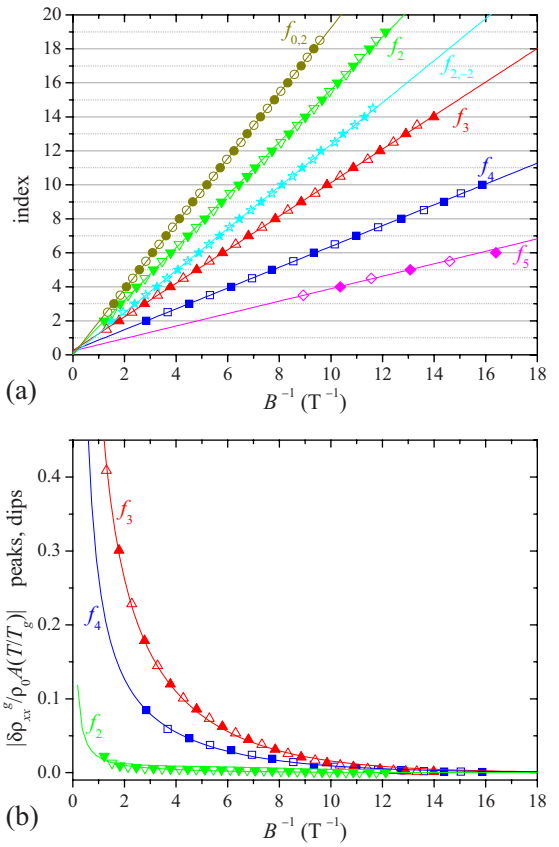

FIG. 6. (Color online) (a) Plots of the index versus position (in the inverse magnetic field) of the extrema of CO Fourier components shown in Fig. 5. The lines are linear fit to the data points. (b) Selected plots of the normalized amplitude versus position of the CO extrema. The curves are the fit to $C/\sinh(B_w/B)$. Maxima and minima are plotted by open and solid symbols, respectively.

difficulty for the components with large enough amplitudes such as f_3 and f_4 in the present case. The scattering parameter $\mu_w=\pi/B_w$ is expected not to vary among components. This is found to be the case for f_3 and f_4; the values obtained by the fitting $\mu_w=10.2$ and 11.3 m^2/Vs, respectively, roughly coincide (within experimental error of $\pm\sim 0.5$ m^2/Vs). For components having smaller amplitudes as f_2 in Fig. 6(b) or other components not plotted in the figure, the two parameter fitting is found to be difficult to perform reliably. In such cases, we resort to the fitting by one parameter C with a fixed B_w taken from the component with the largest amplitude (f_3 in the present case), relying on the invariability of the μ_w. Since only the ratio C/B_w is required for determining the V_g, possible small error in B_w does not affect the resulting V_g very much being compensated for by the responding change in C obtained by the fitting. [Note that $C/\sinh(B_w/B)\sim CB/B_w$ for small B_w/B].

The values of deduced V_g are plotted against $f=(S/2\pi)g$, namely, the values of f_j or $f_{m,n}$ of each component given by Eqs. (7) and (6) in Fig. 7(a) for all the FLSL samples examined in the present work. As can be seen, dominant components are f_4, f_3, or f_2 in most samples. Minor components $f_{2,-2}$ and $f_{0,2}$ are occasionally detected for samples with longer unit lengths. An important factor that controls the modulation amplitude V_g of the component g is the corresponding length (the period) $2\pi/g=S/f$ relative to the depth d of the 2DEG plane, owing to the exponential decay $\propto\exp(-gd)$ along the depth of the effect exerted on the surface. In Fig. 7(b), we replot V_g against S/f. Dominant components for each sample are found to roughly follow the function that fits the modulation amplitude of periodic LSLs with period $a=2\pi/g$ at $n_e=2.8\times10^{15}$ m^{-2},

$$V_g=(-e)\phi_1 e^{-gd}/\epsilon_{\mathrm{TF}}^{\mathrm{FH}}, \tag{8}$$

with $\phi_1=43.8$ meV, $d=100$ nm (the effective depth of the 2DEG that takes account of the average distance of the 2DEG wave function from the heterointerface), and $\epsilon_{\mathrm{TF}}^{\mathrm{FH}}$ representing the dielectric function of 2DEG in the Thomas-Fermi approximation using the Fang-Howard wave function.[49]

Now that we have determined V_g, the profile of the modulated potential can be reconstructed with further supply of the knowledge of the phases ϕ_g. Unfortunately, however, the information of the phases does not manifest itself in the CO as mentioned earlier. We can only surmise the phase of Fourier components by looking into their origin, which is the subject of Sec. IV B. Note, however, that in principle any

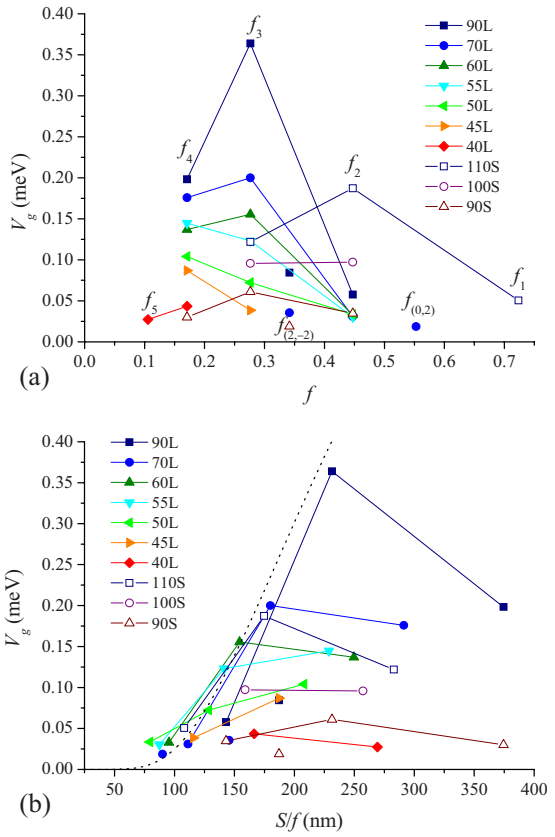

FIG. 7. (Color online) (a) Amplitude of the potential modulation V_g deduced from the CO amplitude for Fourier components specified by f. (b) Replot of (a) against the length S/f corresponding to the Fourier component f. Dotted curve shows amplitude for periodic LSL [Eq. (8)]. Solid and open symbols are used for L-type and S-type samples, respectively. Lines are guides for the eyes and connect only the data points belonging to the principal sequence f_j.

phase relation between an arbitrary pair of components with irrational wave-number ratio can be found at some place in the sequence provided that the sequence is infinitely long.

B. Phase of the Fourier components

In this section, we make an attempt to interpret the origin of the Fourier components observed in the CO. An important property of the Fibonacci sequence to be considered in this respect is its self-similarity. As depicted in the left panel of Fig. 8, the operation of the inflation rule (dividing an L segment into two segments with the ratio of $\tau:1$ to get L and S in the next generation, and renaming an original S segment as L) transforms the Fibonacci sequence to the Fibonacci sequence itself but scaled down by the factor $1/\tau$, while the deflation rule (the inverse process of the inflation) yields the Fibonacci sequence scaled up by the factor τ. The self-similarity implies the presence in a FLSL of multiple length scales scaled to each other successively by the factor τ, where we refer by the term "length scale" to the typical distance between characteristic features that take place repeatedly. The ratio $f_{j+1}/f_j=\tau$ between the adjacent major components f_j can thus be interpreted in terms of the self-similarity.

An obvious example of such repeatedly occurring features is simply the segment S. Recalling that the CO results from the averaging of the square v_d^2 of the drift velocity over the position of the guiding center x_0, it is the spatially averaged distance between the features that is reflected to the frequency B_g of the CO. As depicted in Fig. 8, the distance between the centers of the adjacent S segments is either $2L+S=\tau^3 S$ or $L+S=\tau^2 S$, reflecting the fact that L segments appear in either of the two consecutive (LL) or single isolated (L) form. Noting that the former (the latter) takes place in one-to-one correspondence with the L (S) of the Fibonacci sequence retreating one generation by the deflation process, their relative abundance approaches $\tau:1$ for a long enough sequence. Therefore, the average distance between the centers reads (making use of the relation $\tau^2=\tau+1$)

$$\frac{(\tau^3 S)\tau+(\tau^2 S)}{\tau+1}=(\tau+2)S=\frac{S}{f_3}, \tag{9}$$

accounting for the component f_3 in the CO, which is one of the dominant components in many of the FLSL samples [see Fig. 7(a)]. Since LL is composed of seamless EB resist in L-type samples (seamless open gap in S-type samples), S/f_3 represents as well the average distance between adjacent slabs of the resist or between adjacent free spaces. The values of $\langle \Delta x_{\mathrm{res}} \rangle = S/f_3$ for the samples examined in the present study are tabulated in Table I. Other principal components f_j can roughly be viewed as deriving from the inflation or deflation of f_3. More specifically f_1, f_2, f_4, and f_5 are attributable to the centers of both types of the segments, the L segments, the LL's, and the isolated L's, respectively (see Fig. 8). The minor components $f_{m,n}$ not categorized in f_j can be ascribed to the edges of the resist slabs, which basically bear the frequency twice of the corresponding major components.

To gain insight into the phase of the modulation, we need to take a closer look at the position of the characteristic features. Since the kth appearance ($k=1,2,3,\ldots$) of the L segment (S segment) takes place at the a_kth (b_kth) place in the whole sequence, where $a_k=k+\mathrm{Int}(k/\tau)$ and $b_k=2k+\mathrm{Int}(k/\tau)$ represent a pair of Beatty sequences[56] with $\mathrm{Int}(x)$ denoting the integer part of x, the position of the kth center of the S segment [indicated by (red) vertical lines in the central panel of Fig. 8] is given by

$$x_k^S=(b_k-k)\tau S+kS-\frac{S}{2}=\left[\frac{k}{f_3}-\tau\mathrm{Frac}\left(\frac{k}{\tau}\right)-\frac{1}{2}\right]S, \tag{10}$$

with $\mathrm{Frac}(x)=x-\mathrm{Int}(x)$ denoting the fractional part of x. The positions of other features can be written down along the same line, exploiting the correspondence of the feature to L or S in the inflated or deflated Fibonacci sequence and tabulated in Table II—employing S as the unit of the length. We used the notation $k^+=k+[1-(-1)^k]/2$ in the description of the minor components, which takes the same number for an odd k and the subsequent even k.

Since τ is an irrational number, $\mathrm{Frac}(k/\tau)$ and $\mathrm{Frac}(k^+/2\tau)$ take the value uniformly distributed in the interval $[0,1)$ fluctuating with k around the central value 1/2. The distance between the features under consideration, seen by the electrons traveling in the cyclotron orbit, fluctuates accordingly

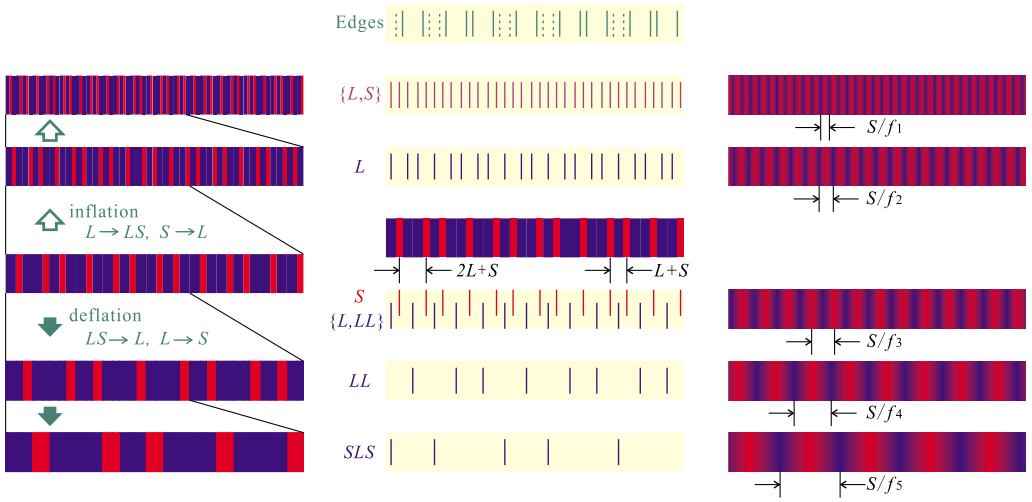

FIG. 8. (Color online) Center: Diagram that sketches the Fibonacci sequence [L and S are represented by dark (blue) and bright (red) rectangles, respectively] with the vertical lines above and below indicating the locations of characteristic features: the centers of the segments not discriminating their types ($\{L,\ S\}$), the centers of the L segments (L), the centers of the S segments (S), the centers of the L areas counting the two consecutive L's, LL, as a single area ($\{L,\ LL\}$), the centers of LL's only (LL), and the centers of single isolated L's surrounded by S's on both sides (SLS). The boundaries between L and S segments (denoted as $|S|$ with the $|$'s symbolizing the edges) are displayed in the top panel. The edges $|S|$ can be categorized into two groups, namely, the edges between LL and S ($|LL|$) and between isolated L and S ($S|L|S$), which are shown by solid and dashed lines, respectively. Right: Schematic representation of the Fourier component (the "average" *periodic* modulation) originating from the characteristic feature depicted to the left. Left: The inflation and the deflation of the Fibonacci sequence.

with the guiding center position x_0. In the context of the CO, we only need the average of the value over x_0. Therefore the fractional parts in Table II can be replaced by their average 1/2, resulting in the spatially averaged locations $\langle x\rangle$ tabulated in Table III. For the components deriving from the edges, we noted that $(-1)^k$ vanishes on averaging and hence $k^+ \to k+1/2$ and also used the relations $f_{0,2}=2f_3$, $f_{2,-2}=2f_4$, and $f_{-2,4}=2f_5$.

For the reconstruction of the potential profile, it is necessary to further relate the characteristic features discussed thus far to the potential modulation they create. This requires detailed knowledge of the strain introduced into the GaAs/AlGaAs wafer by the resist slabs, which is beyond the reach of the present study. Here we simply assume that the potential energy becomes higher at the 2DEG areas directly beneath the resist slabs, namely, at L sites (S sites) for L-type (S-type) samples, which are probably under compressive strain. Accordingly, the Fourier components including their phases are written (referring to Table III) as $\pm V_j \cos[2\pi f_j(x/S+\tau^2/2)]$ for $j=2$, 4, and 5 and $\mp V_3 \cos[2\pi f_3(x/S+\tau^2/2)]$ for $j=3$ with the upper (lower) sign for L-type (S-type) samples. For the component f_1, which includes L sites and S sites alike, we presume that the L sites dominate the sign $\pm V_1 \cos[2\pi f_1(x/S+1/\tau)]$. For edges, we assign the sign opposite to the area in between, namely, $\pm V_{0,2} \cos[4\pi f_3(x/S+\tau/4)]$ and $\mp V_{2,-2} \cos[4\pi f_4(x/S-1/4\tau)]$; the component $f_{-2,4}$ was not observed in the present experiment.

The modulation profile is obtained by adding up all the components observed in the experiment. Examples of the profiles thus reconstructed, as well as the constituent Fourier components, are displayed in Figs. 9 and 10 for L-type (50 and 70L) and S-type (90 and 110S) samples, respectively, using the phases assumed above. It is intriguing to note that

TABLE II. The x coordinate of the kth appearance of characteristic features defined in Fig. 8.

	Location (in unit S)
$x_k^{\{L,S\}}$	$k/f_1-(1/2\tau)\{1+\mathrm{Frac}[(k+1)/\tau]+\mathrm{Frac}(k/\tau)\}$
x_k^{L}	$k/f_2-\tau/2-\mathrm{Frac}(k/\tau)$
x_k^{S}	$k/f_3-1/2-\tau\mathrm{Frac}(k/\tau)$
x_k^{LL}	$k/f_4-\tau^2\mathrm{Frac}(k/\tau)$
x_k^{SLS}	$k/f_5+\tau/2-\tau^3\mathrm{Frac}(k/\tau)$
$x_k^{\lvert S\rvert}$	$k^+/f_{0,2}-\tau\mathrm{Frac}(k^+/2\tau)-0^+$
$x_k^{\lvert LL\rvert}$	$k^+/f_{2,-2}-\tau^2\mathrm{Frac}(k^+/2\tau)+(-1)^k\tau$
$x_k^{S\lvert L\rvert S}$	$k^+/f_{-2,4}-\tau^3\mathrm{Frac}(k^+/2\tau)+0^+\tau$

TABLE III. The spatially averaged location of x_k's given in Table II for infinitely long sequence.

	Location (in unit S)
$\langle x_k^{\{L,S\}}\rangle$	$k/f_1-1/\tau$
$\langle x_k^{L}\rangle$	$k/f_2-\tau^2/2$
$\langle x_k^{S}\rangle$	$k/f_3-\tau^2/2$
$\langle x_k^{LL}\rangle$	$k/f_4-\tau^2/2$
$\langle x_k^{SLS}\rangle$	$k/f_5-\tau^2/2$
$\langle x_k^{\lvert S\rvert}\rangle$	$(k+1/2)/2f_3-\tau^2/2$
$\langle x_k^{\lvert LL\rvert}\rangle$	$(k+1/2)/2f_4-\tau^2/2$
$\langle x_k^{S\lvert L\rvert S}\rangle$	$(k+1/2)/2f_5-\tau^2/2$

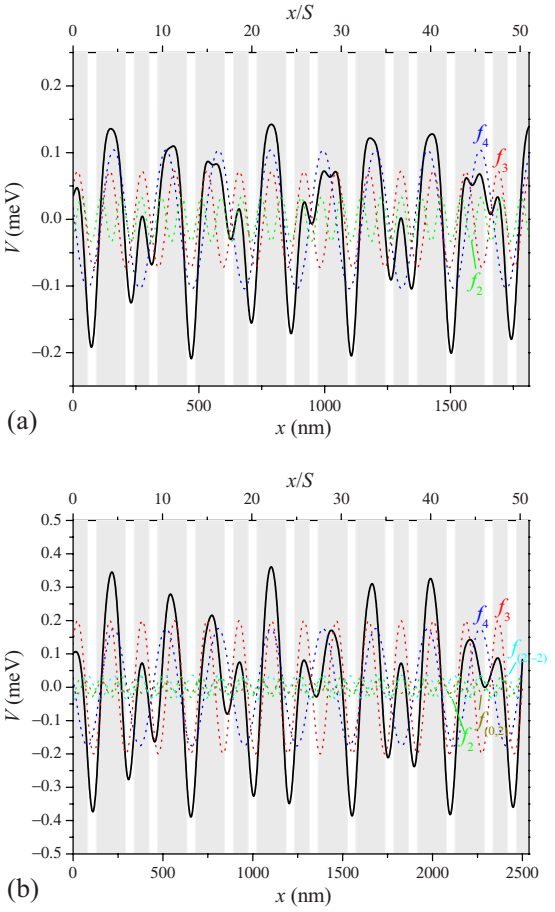

FIG. 9. (Color online) Potential profile of FLSLs (solid lines) reconstructed by the superposition of the Fourier components (dotted lines) with the amplitudes determined by the analysis of the CO and the phase obtained from the consideration of the origin of the components for L-type samples 50L (a) and 70L (b). Note the difference in both vertical and horizontal scales. The horizontal axis is scaled so as to keep x/S (top axis) the same for both figures. The shades indicate the area in the 2DEG plane located right beneath the resist, namely, the L sites.

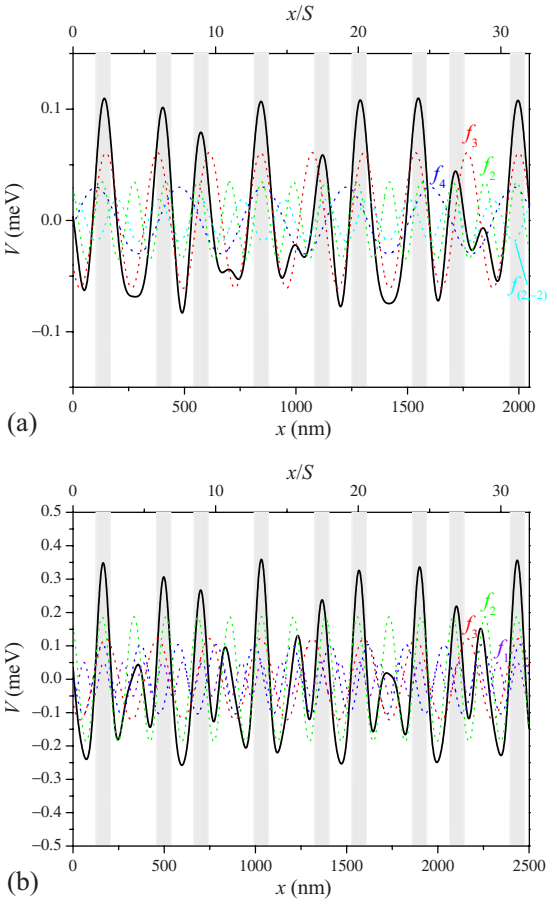

FIG. 10. (Color online) Similar to Fig. 9 for S-type samples 90S (a) and 110S (b). The shades indicate the S sites.

the superposition of a small number of incommensurate periodic sinusoidal modulations basically reproduce the quasiperiodic profile. Because of the low-pass filtering action of the attenuation $\exp(-gd)=\exp[-(2\pi f/S)d]$ mentioned earlier, higher frequency components (components f_j with smaller j), i.e., the components with shorter length scale, are damped heavier for samples with smaller S. This is reflected in the difference of the profile between samples, resulting in rather dull line shape for samples with smaller S when plotted against x scaled by the unit length S (see the top axes). The profile of S-type samples is qualitatively similar to that of L-type samples but laid upside down. Quantitatively, however, the modulation amplitude of S-type samples is much smaller than that of corresponding L-type samples with the same set of length units L and S (compare samples 90L and 90S in Fig. 7). This is attributable to $1/\tau$ times smaller coverage by the resist slabs of the surface that exerts much smaller strain to the underlying GaAs/AlGaAs 2DEG wafer.

V. DISCUSSION

What we have shown in Secs. II–IV demonstrate that the Fourier analysis of the CO serves as a useful tool to probe the complicated profile of the modulated potential introduced into a 2DEG. FLSLs contain a number of Fourier components and therefore provide archetypal proving ground for the technique. The method, however, can be applied in wider range of systems that are comprised of multiple Fourier contents, e.g., periodic systems that retain higher harmonics. The technique is—in a sense—analogous to diffraction techniques that determine the crystal structures. In fact, Eq. (5) with Eq. (1) closely resembles the Patterson function[57] $P(x)=\Sigma_g(|V_g|^2/2)\cos(gx)$ by replacing $x=2R_c^*=2R_c-\pi/2g$ and, therefore, can roughly be viewed as the autocorrelation function of the modulated potential measured by the cyclotron diameter with offset $2R_c^*$. In this section, we discuss the limitations of the CO as a technique to determine the "structure" of the modulated potential.

First, the information on the phase of the Fourier components is lost from the CO, which has been discussed so far. Again this resembles the situation in the diffraction techniques; the phases are unavailable in the diffraction pattern, which records only the intensity of the diffraction spots. In both cases, the phases have to be estimated from the symmetry of the system or from the physical origin of the compo-

nent, which has been done in Sec. IV. This can be a major source of uncertainty in the obtained reconstructed structures. Note, however, that the knowledge of the intensity of Fourier contents (without their phase interrelation) suffices for their explanation in many phenomena, a representative example being—of course—the CO itself.

Second, because of the thermal damping factor $A(T/T_g)$ in Eq. (1) that decreases with increasing g, the CO is less sensitive to components with larger g, i.e., to shorter length scales. Therefore, higher frequency components can be overlooked in CO traces especially in those taken at higher temperatures. In principle, complementary use of the geometric resonance of the open orbit,[15] which is a sensitive probe to higher frequency components,[58] can fill the gap. However, the amplitude of the open-orbit resonance still remains unexplained quantitatively and its application to the determination of the modulation amplitude is yet to be explored. Conversely, the requirement for the electrons to travel at least one cycle of the cyclotron orbit before being scattered sets an ultimate upper limit in the length scale that can be examined by the CO, which roughly equals the mean-free path. Practical upper limit will be smaller than this and will be reached when the oscillation resulting from the length scale becomes indistinguishable from the slowly varying background (when the peak becomes indiscernible in the Fourier spectrum as shown in Fig. 4 due to the low-pass-filtering action of the operation of d^2/dB^2). Therefore, the modulation profile may possibly contain higher or lower frequency components that elude the detection by the CO.

Before concluding the paper, we briefly discuss the prospective use of a FLSL as a system to experimentally test the exotic properties in quasiperiodic systems that are theoretically predicted.[22–24] The capability to experimentally determine the profile of the potential experienced by the electrons is obviously of great advantage to this end. However, further improvement of the sample that enables to control the electron density is desirable since it will be necessary for many purposes to vary the Fermi energy or the Fermi wave number in detail. In 2DEG-based devices, this can generally be achieved by implementing a uniform gate. Note that in LSLs we have to resort to a back gate, since the front surface of the wafer is occupied by the grating that introduces the modulation. For back-gated LSLs, it was found that the modulation amplitude shows strong increase accompanying the decrease in the electron density by the application of the negative gate bias,[59] which might complicate the interpretation of the data obtained by the experiments. A project to develop LSLs with conducting resist gratings that can be biased to compensate for the change in the modulation amplitude induced by the back-gate bias is now under progress. Another caveat to be born in mind is that our FLSLs are basically a 2D system where electrons can travel both parallel and perpendicular to the 1D modulation. In many theories, by contrast, strictly 1D systems are considered. It may therefore be necessary for some purposes to start the device fabrication from a quantum wire instead of a plain 2DEG.

VI. CONCLUSIONS

We have shown that the complicated CO observed in a FLSL can be decomposed into the constituent Fourier components by applying a numerical band-pass filter with the aid of numerical operation of d^2/dB^2 for background elimination (and later integration by B twice for recovery). From the amplitude of the component thus isolated, the magnitude V_g of the potential modulation responsible for the component can be determined. The analysis reveals that the potential profile seen by the electrons in a FLSL is basically described by the superposition of a small number of incommensurate periodic modulations. The periods of the major components are given by S/f_j with f_j in Eq. (7) and are explicable in terms of inflation and deflation rules that lead to the self-similarity. By examining the physical origin of the components, we can estimate the phase of each component, which allows us to reconstruct the modulation profile. With the detailed knowledge of the potential profile, we believe that a FLSL provides an excellent arena to experimentally explore exotic phenomena (localization, critical wave functions, a Cantor-set spectrum, etc.) envisaged in the quasiperiodic systems.

ACKNOWLEDGMENTS

This work was supported by the Grant-in-Aid for Scientific Research (C) (No. 18540312) and (A) (No. 18204029) from the Ministry of Education, Culture, Sports, Science and Technology, Japan.

*akrendo@issp.u-tokyo.ac.jp; http://iye.issp.u-tokyo.ac.jp/endo/

[1] C. W. J. Beenakker and H. van Houten, in *Solid State Physics*, edited by H. Ehrenreich and D. Turnbull (Academic, San Diego, 1991), Vol. 44, p. 1.

[2] P. H. Beton, E. S. Alves, P. C. Main, L. Eaves, M. W. Dellow, M. Henini, O. H. Hughes, S. P. Beaumont, and C. D. W. Wilkinson, Phys. Rev. B **42**, 9229 (1990).

[3] D. Weiss, K. v. Klitzing, K. Ploog, and G. Weimann, Europhys. Lett. **8**, 179 (1989).

[4] R. W. Winkler, J. P. Kotthaus, and K. Ploog, Phys. Rev. Lett. **62**, 1177 (1989).

[5] A. K. Geim, R. Taboryski, A. Kristensen, S. V. Dubonos, and P. E. Lindelof, Phys. Rev. B **46**, 4324 (1992).

[6] G. Müller, D. Weiss, K. von Klitzing, P. Streda, and G. Weimann, Phys. Rev. B **51**, 10236 (1995).

[7] M. Tornow, D. Weiss, A. Manolescu, R. Menne, K. v. Klitzing, and G. Weimann, Phys. Rev. B **54**, 16397 (1996).

[8] B. Milton, C. J. Emeleus, K. Lister, J. H. Davies, and A. R. Long, Physica E (Amsterdam) **6**, 555 (2000).

[9] A. Endo and Y. Iye, Phys. Rev. B **66**, 075333 (2002).

[10] A. Endo and Y. Iye, Physica E (Amsterdam) **22**, 122 (2004).

[11] J. H. Smet, S. Jobst, K. von Klitzing, D. Weiss, W. Wegscheider, and V. Umansky, Phys. Rev. Lett. **83**, 2620 (1999).

[12] R. L. Willett, K. W. West, and L. N. Pfeiffer, Phys. Rev. Lett. **83**,

2624 (1999).
[13] A. Endo, M. Kawamura, S. Katsumoto, and Y. Iye, Phys. Rev. B **63**, 113310 (2001).
[14] R. A. Deutschmann, W. Wegscheider, M. Rother, M. Bichler, G. Abstreiter, C. Albrecht, and J. H. Smet, Phys. Rev. Lett. **86**, 1857 (2001).
[15] A. Endo and Y. Iye, Phys. Rev. B **71**, 081303(R) (2005).
[16] R. R. Gerhardts, D. Weiss, and U. Wulf, Phys. Rev. B **43**, 5192 (1991).
[17] T. Schlösser, K. Ensslin, J. P. Kotthaus, and M. Holland, Europhys. Lett. **33**, 683 (1996).
[18] C. Albrecht, J. H. Smet, D. Weiss, K. von Klitzing, R. Hennig, M. Langenbuch, M. Suhrke, U. Rössler, V. Umansky, and H. Schweizer, Phys. Rev. Lett. **83**, 2234 (1999).
[19] M. C. Geisler, J. H. Smet, V. Umansky, K. von Klitzing, B. Naundorf, R. Ketzmerick, and H. Schweizer, Phys. Rev. Lett. **92**, 256801 (2004).
[20] S. Chowdhury, A. R. Long, E. Skuras, J. H. Davies, K. Lister, G. Pennelli, and C. R. Stanley, Phys. Rev. B **69**, 035330 (2004).
[21] See, e.g., E. Maciá, Rep. Prog. Phys. **69**, 397 (2006), for a recent review.
[22] S. Aubry and G. Andre, Ann. Isr. Phys. Soc. **3**, 133 (1980).
[23] J. B. Sokoloff, Phys. Rep. **126**, 189 (1985).
[24] M. Kohmoto, B. Sutherland, and C. Tang, Phys. Rev. B **35**, 1020 (1987).
[25] R. Merlin, K. Bajema, R. Clarke, F. Y. Juang, and P. K. Bhattacharya, Phys. Rev. Lett. **55**, 1768 (1985).
[26] J. Todd, R. Merlin, R. Clarke, K. M. Mohanty, and J. D. Axe, Phys. Rev. Lett. **57**, 1157 (1986).
[27] A. A. Yamaguchi, T. Saiki, T. Tada, T. Ninomiya, K. Misawa, T. Kobayashi, M. K. Gonokami, and T. Yao, Solid State Commun. **75**, 955 (1990).
[28] W. Gellermann, M. Kohmoto, B. Sutherland, and P. C. Taylor, Phys. Rev. Lett. **72**, 633 (1994).
[29] D. Munzar, L. Bočáek, J. Humlíček, and K. Ploog, J. Phys.: Condens. Matter **6**, 4107 (1994).
[30] D. Toet, M. Potemski, Y. Y. Wang, J. C. Maan, L. Tapfer, and K. Ploog, Phys. Rev. Lett. **66**, 2128 (1991).
[31] P. Mikulík, V. Holý, J. Kuběna, and K. Ploog, Acta Crystallogr., Sect. A: Found. Crystallogr. **51**, 825 (1995).
[32] Y. Y. Zhu, N. B. Ming, and W. H. Jiang, Phys. Rev. B **40**, 8536 (1989).
[33] L. Macon, J. P. Desideri, and D. Sornette, Phys. Rev. B **44**, 6755 (1991).
[34] K. Kono, S. Nakada, Y. Narahara, and Y. Ootuka, J. Phys. Soc. Jpn. **60**, 368 (1991).
[35] S. Katsumoto, N. Sano, and S. Kobayashi, Solid State Commun. **85**, 223 (1993).
[36] A. R. Smith, K. Chao, Q. Niu, and C. Shih, Science **273**, 226 (1996).
[37] P. Ebert, K. J. Chao, Q. Niu, and C. K. Shih, Phys. Rev. Lett. **83**, 3222 (1999).
[38] P. Moras, W. Theis, L. Ferrari, S. Gardonio, J. Fujii, K. Horn, and C. Carbone, Phys. Rev. Lett. **96**, 156401 (2006).
[39] D. Eom, C. S. Jiang, H. B. Yu, J. Shi, Q. Niu, P. Ebert, and C. K. Shih, Phys. Rev. Lett. **97**, 206102 (2006).
[40] A. Endo and Y. Iye, in *Physics of Semiconductors*, AIP Conf. Proc. No. 893 (AIP, Melville, New York, 2007), p. 575.
[41] A. Endo and Y. Iye, Physica E (Amsterdam) **40**, 1145 (2008).
[42] A. Endo, S. Katsumoto, and Y. Iye, Phys. Rev. B **62**, 16761 (2000).
[43] The formula is for $B>0$. For $B<0$, B should be replaced with $-B$ in this and other formulas hence presented.
[44] C. W. J. Beenakker, Phys. Rev. Lett. **62**, 2020 (1989).
[45] A. D. Mirlin and P. Wölfle, Phys. Rev. B **58**, 12986 (1998).
[46] C. Zhang and R. R. Gerhardts, Phys. Rev. B **41**, 12850 (1990).
[47] F. M. Peeters and P. Vasilopoulos, Phys. Rev. B **46**, 4667 (1992).
[48] R. R. Gerhardts, Phys. Rev. B **45**, 3449 (1992).
[49] A. Endo and Y. Iye, J. Phys. Soc. Jpn. **74**, 2797 (2005).
[50] E. Skuras, A. R. Long, I. A. Larkin, J. H. Davies, and M. C. Holland, Appl. Phys. Lett. **70**, 871 (1997).
[51] D. Levine and P. J. Steinhardt, Phys. Rev. B **34**, 596 (1986).
[52] V. Elser, Acta Crystallogr., Sect. A: Found. Crystallogr. **42**, 36 (1986).
[53] In a simple case where the lattice points in the original 2D square lattice are all identical, the structure factor reads (Ref. 52) $S(z) \propto \sin(z)/z$ with $z=\pi\tau|-m+n\tau|/\sqrt{5}$ and therefore becomes large when $m/n \sim \tau$. Although the case does not exactly apply to our FLSLs, it hints at larger amplitude for m and n given by two consecutive Fibonacci numbers.
[54] R. A. Dunlap, *The Golden Ratio and Fibonacci Numbers* (World Scientific, Singapore, 1997).
[55] A. S. Posamentier and I. Lehmann, *The Fabulous Fibonacci Numbers* (Prometheus Books, New York, 2007).
[56] M. R. Shroeder, *Fractals, Chaos, Power Laws* (Freeman, New York, 1991).
[57] J. M. Cowley, *Diffraction Physics* (North-Holland, Amsterdam, 1981).
[58] A. Endo and Y. Iye, Physica E (Amsterdam) **34**, 640 (2006).
[59] A. Endo and Y. Iye, J. Phys. Soc. Jpn. **74**, 1792 (2005).